



# Amino acid-derived non-precious catalysts with excellent electrocatalytic performance and methanol tolerance in oxygen reduction reaction

Da-Hee Kwak, Sang-Beom Han, Do-Hyoung Kim, Ji-Eun Won, Kyung-Won Park\*

Department of Chemical Engineering, Soongsil University, Seoul 156-743, Republic of Korea



## ARTICLE INFO

### Keywords:

Cysteine  
Doped carbon nanostructure  
Non-precious metal catalyst  
Oxygen reduction reaction  
Methanol tolerance

## ABSTRACT

In polymer electrolyte membrane fuel cells (PEMFCs), slow kinetics and high over-potential of oxygen reduction reaction (ORR) can result in a significantly large amount of Pt usage. Thus, non-precious metal (NPM) catalysts, especially, for ORR, that can be utilized instead of Pt-based catalysts, have been intensively studied. Herein, doped carbon nanostructures as NPM catalysts for ORR in an acid medium were synthesized using a template method with nontoxic, eco-friendly cysteine and iron (III) tetramethoxyphenylporphyrin (Fe-TMPP, 5,10,15,20-tetrakis(4-methoxyphenyl)-21H,23H-porphyrin iron(III) chloride) used as carbon and doping sources, respectively. To obtain the doped mesoporous carbon nanostructure, mixtures of cysteine and Fe-TMPP with intended ratios (Cys<sub>x</sub>/Fe<sub>z</sub>) were heated under an N<sub>2</sub> atmosphere at 900 °C for 3 h. In particular, Cys<sub>2</sub>/Fe<sub>0.3</sub>/C synthesized with an appropriate ratio of cysteine and Fe-TMPP showed a relatively high specific surface area and fairly high portion of doped species such as pyridinic and pyrrolic N, thiophenic S, and Fe-N<sub>x</sub>. Moreover, Cys<sub>2</sub>/Fe<sub>0.3</sub>/C exhibited significantly enhanced ORR activity and stability in 0.5 M H<sub>2</sub>SO<sub>4</sub> and superior tolerance of methanol in 0.5 M H<sub>2</sub>SO<sub>4</sub> in the presence of CH<sub>3</sub>OH.

## 1. Introduction

Polymer electrolyte fuel cells (PEMFCs) are eco-friendly electrochemical energy conversion systems with critical advantages such as a relatively low operating temperature, low-emission of pollutants, and high power density [1–3]. However, despite these merits, the high price and limited reserves of platinum (Pt) catalyst used as the anode and cathode hinder the commercialization of PEMFCs [4–7]. In particular, the slow kinetics and high over-potential of oxygen reduction reaction (ORR) are responsible for a significantly larger amount of Pt usage compared to an anode for hydrogen reduction reaction [8–10]. Thus, since the cost reduction of a membrane electrode assembly (MEA) having high efficiency and improved durability needs to be preferentially resolved, non-precious metal (NPM) catalysts, especially, for ORR, that can be utilized instead of Pt-based catalysts, have been intensively studied [11–15].

For the NPM cathode catalysts for ORR in PEMFCs, carbon nanostructures doped with heteroatoms as dopants such as nitrogen, sulfur, and phosphorous have been extensively proposed [16–20]. With a similar atomic size to that of carbon (C), nitrogen (N) has been known as a promising n-type dopant, i.e. an electron donor, which can improve the electrical conductivity and affect the structural and electrochemical properties of carbon structures [21,22]. Due to an increased surface

polarity of the carbon surrounded by nitrogen, the N-doped carbon structure might have a rapid charge transfer rate and improved proton/electron transfer, thus exhibiting enhanced ORR activity with decreased overpotential and facilitated adsorption of oxygen molecules [23,24]. The active sites for ORR in the N-doped carbon structure are pyridinic and pyrrolic nitrogen states, which exist at the edge of graphite [25]. The pyridinic and pyrrolic-N states with non-bonded extra-electrons can facilitate the adsorption of oxygen and the formation of M-N<sub>4</sub> with metals such as Fe and Co [26–28]. The doping of sulfur (S) into a carbon structure can cause deformation, open edge, and high curvature, resulting in a high specific surface area. The defect sites in carbon-based catalysts might induce a facile adsorption of oxygen molecules, exhibiting an improved ORR activity [21,29,30]. Recently, compared to the singular doping of the heteroatom, the carbon nanostructures formed by dual doping of N and S showed significantly enhanced ORR performance [31–33]. The synergistic effect of the co-doping on the ORR might result from the increased catalytic active sites, which could facilitate the accessibility of oxygen molecules to the dopant site.

The macrocyclic N<sub>4</sub> ligand used as a NPM cathode catalyst for ORR was proposed in 1964 [34]. The carbon-supported macrocyclic N<sub>4</sub> compounds synthesized at 500–1000 °C were studied, and were shown to exhibit a more active, stable NPM catalytic activity. Recently, carbon nanostructures having M-N<sub>x</sub> (M = Fe, Co) complex were prepared by

\* Corresponding author.

E-mail address: [kwpark@ssu.ac.kr](mailto:kwpark@ssu.ac.kr) (K.-W. Park).

pyrolysis of mixtures consisting of metal salts, carbon, and nitrogen precursors at a high temperature under an inert gas atmosphere [35,36]. To further obtain doped carbon nanostructures as promising NPM cathode catalysts for enhanced ORR performance, metal-phthalocyanine (M-Pc) and metal-porphyrin (M-TMPP) having macrocyclic M-N<sub>4</sub> structures have been utilized as carbon, nitrogen and metal sources [37–39]. The M-N<sub>4</sub> structures formed with M-Pc and M-TMPP in the doped carbon catalysts can act as active catalytic sites, inducing a highly graphitic structure with an enhanced electrical conductivity and stability. Although the role of the transition metal in the M-N<sub>4</sub> structures for the ORR are still controversial, the doped carbon catalysts containing the M-N<sub>4</sub> structures showed the improved ORR activity, compared with the N<sub>x</sub> structures [40,41]. In this study, to clarify the possible origins of catalytically active sites for the ORR activity, co-doped carbon nanostructure catalysts were synthesized using different mixtures of cysteine (C<sub>3</sub>H<sub>7</sub>NO<sub>2</sub>S) and metal-porphyrin. Moreover, in direct methanol fuel cells (DMFCs), NPM cathode catalysts have shown superior tolerance to cross-over methanol, compared to Pt/C catalysts [11]. However, the NPM catalysts with M-N<sub>4</sub> structures have generally been prepared using expensive, toxic, or flammable chemicals such as Fe-Pc, Fe-TMPP, acetonitrile, ammonia, and urea [21]. Herein, among inexpensive and stable amino acids, co-doped carbon nanostructures were synthesized with cysteine (C<sub>3</sub>H<sub>7</sub>NO<sub>2</sub>S) containing S as well as N and C utilized as sulfur, nitrogen and carbon sources at 900 °C under an N<sub>2</sub> atmosphere. The NPM catalysts prepared using cysteine as the main source with a silicate template (SBA-15) exhibited a mesoporous nanostructure with a fairly high specific surface area, improved ORR activity, and enhanced tolerance of methanol in an acid medium.

## 2. Experimental

### 2.1. Synthesis of iron, nitrogen, and sulfur doped mesoporous carbon catalysts

To prepare a silica template (SBA-15), pluronic P123 (0.8 g, P123 triblock copolymer (EO<sub>20</sub>PO<sub>70</sub>EO<sub>20</sub>), Sigma Aldrich) was dissolved in 2 M HCl (35.0 ~ 37.0%, SAMCHUN) solution. Tetraethyl orthosilicate (TEOS, 17 g, Sigma Aldrich) was then added to the mixed solution at 35 °C with continuous stirring for 20 h and aged at 80 °C for 24 h. After the aging process, the precipitate was washed with de-ionized (DI) water and ethanol, and then dried in a 50 °C oven for 12 h. Finally, an SBA-15 template was obtained by heating at 600 °C for 4 h under an air atmosphere. To obtain the doped mesoporous carbon nanostructure, L-cysteine (Sigma Aldrich) and Fe-TMPP (5,10,15,20-tetrakis(4-methoxyphenyl)-21H,23H-porphyrin iron(III) chloride, Sigma Aldrich) with an intended ratio were homogeneously mixed with SBA-15 for 15 min using a mortar. The mixed powder was heated at 900 °C for 3 h under an N<sub>2</sub> atmosphere. The heated sample was stirred in 10 vol.% hydrofluoric (HF) acid solution (J.T Baker) for 2 h, washed with DI water and ethanol, and then dried in a 50 °C oven for 12 h.

### 2.2. Structural analysis of catalysts

The morphology and chemical composition of the samples were analyzed using correction scanning transmission electron microscopy (Cs-corrected STEM, JEOL, JEM-ARM 200 F) and energy dispersive X-ray spectrometry (EDX). The crystal structure of the samples was confirmed using the X-ray diffraction (XRD, Bruker D2 Phase system) method at 30 kV and 10 mA with a Cu K<sub>α</sub> source ( $\lambda = 0.15406 \text{ \AA}$ ) and Ni filter. The crystallinity of the samples was characterized using a high resolution Raman spectrometer (Horiba Jobin Yvon, LabRAM HR UV/Vis/NIR photoluminescence). The specific surface area and pore structure were obtained from nitrogen adsorption and desorption isotherms measured using a Micromeritics ASAP 2020 analyzer. The crystallinity of the samples was characterized using a high resolution Raman spectrometer (Horiba Jobin Yvon, LabRAM HR UV/Vis/NIR

photoluminescence). The structural features of the samples were observed using Fourier transform infrared (FT-IR, Bruker, Vertex70) analysis at attenuated total reflection mode. Thermal gravimetric analysis (TGA, TA Instrument, SDT Q600) and differential scanning calorimetry (DSC, TA Instrument, SDT Q600) were performed in the temperature range of 30–900 °C under an N<sub>2</sub> atmosphere to investigate the thermal properties of the precursors. To analyze the chemical states and composition of the samples, X-ray photoelectron spectroscopy (XPS, Thermo Scientific, K-Alpha) was utilized under a chamber pressure of  $7.8 \times 10^{-9}$  Torr with a beam power of 200 W and Al K<sub>α</sub> X-ray source of 1468.8 eV.

### 2.3. Electrochemical analysis of catalysts

The electrochemical properties of the samples were characterized using a potentiostat (CH Instrument, CHI 700C) in a three-electrode electrochemical cell at room temperature. Ag/AgCl (saturated in 3 M KCl) and a graphite rod were used as the reference and counter electrodes, respectively. The catalyst ink for electrochemical analysis was prepared by homogeneously mixing the sample, isopropanol (Sigma Aldrich), and 5 wt.% Nafion<sup>®</sup> solution (Sigma Aldrich) with continuous ultrasonication. The prepared catalyst ink was dropped on a glassy carbon rotating disk electrode with an amount of  $600 \text{ \mu g}_{\text{catalyst}} \text{ cm}^{-2}$  and dried in a 50 °C oven for 10 min. For comparison, a commercial Pt catalyst (20 wt.% Pt/Vulcan XC-72, Premetek Co.) was utilized. Cyclic voltammograms (CVs) and linear sweep voltammograms (LSVs) of the samples were obtained in Ar or O<sub>2</sub>-saturated 0.5 M H<sub>2</sub>SO<sub>4</sub> at a scan rate of 50 mV s<sup>-1</sup> and 1 mV s<sup>-1</sup>. To evaluate the catalytic durability of the samples for ORR, linear sweep voltammetry was performed by cycling in the potential range of 0.7–1.2 V (vs. reversible hydrogen electrode (RHE)) at a scan rate of 50 mV s<sup>-1</sup>. The role of iron as an active site in the doped carbon nanostructure was confirmed by comparing the LSVs in O<sub>2</sub>-saturated 0.5 M H<sub>2</sub>SO<sub>4</sub> + 10 mM potassium cyanide (KCN) solution with those in O<sub>2</sub>-saturated 0.5 M H<sub>2</sub>SO<sub>4</sub> solution. The methanol tolerance of the doped carbon nanostructures for cathode catalysts used in direct methanol fuel cells was characterized by comparing the LSVs in O<sub>2</sub>-saturated in the presence of different concentrations of CH<sub>3</sub>OH. All electrode potentials were converted to RHE.

### 2.4. Fabrication of membrane electrode assembly (MEA) and unit cell measurement

The MEA for unit cell measurement was fabricated using the NPM cathode catalysts for ORR. The cathode (~3.5 mg cm<sup>-2</sup>) was fabricated on a Teflon film using a decal method with catalyst inks, which were prepared by mixing catalyst powder (0.2 g) with de-ionized water (300  $\mu$ L), isopropanol alcohol (4725  $\mu$ L, Sigma Aldrich), and 5 wt% Nafion<sup>®</sup> solution (3250  $\mu$ L, Sigma Aldrich). The as-prepared cathode was transferred to a Nafion<sup>®</sup> membrane (211, Dupont). The Pt(20 wt%) catalyst on carbon black (~0.5 mg<sub>Pt</sub> cm<sup>-2</sup>) was utilized as an anode. The MEA was fabricated by hot pressing with an anode and cathode on a Nafion<sup>®</sup> membrane at 120 °C under a pressure of 100 bar for 2 min. The as-prepared MEA for the PEMFC was inserted into graphite plates with a serpentine flow field (an active area of 5 cm<sup>2</sup>). The PEMFC performance was evaluated with a computer-controlled electronic load (CNLPEM005-01, CNL Energy Co.) at 80 °C under an ambient pressure. H<sub>2</sub> as a fuel and O<sub>2</sub> as an oxidant humidified at 80 °C were supplied with flow rates of 200 and 500 mL min<sup>-1</sup> at the anode and cathode, respectively. In the DMFC measurement, the MEA was fabricated by hot pressing with an anode (PtRu black) and cathode (Cys2/Fe0.3/C) on the Nafion<sup>®</sup> membrane (212, DuPont) at 120 °C under a pressure of 100 bar for 2 min. Cell performance was evaluated at 65 °C and the flow rate of the 2 M, 5 M and 10 M methanol solution at the anode was 2 mL min<sup>-1</sup>. The flow rates of O<sub>2</sub> gas (humidified at 60 °C) was 500 mL min<sup>-1</sup>.

## 2.5. Density functional theory (DFT) calculations

Density functional theory (DFT) calculations were carried out with Quantum-ESPRESSO code [42]. The wave functions and charge density were expanded within plane wave basis sets with cut-off kinetic energies of 60 and 240 Rydberg, respectively. The interaction between the electron and nucleus was expressed with norm-conserving pseudopotentials and the exchange-correlation of the electron was approximated by Perdew-Burke-Ernzerhof functional [43,44]. To model graphene quantum dot systems, we used a supercell comprising 30 carbon atoms passivated by hydrogen atoms as the starting model. To avoid the interactions of the prepared supercell with periodically repeated cells, 12 Å-thick vacuum layers were placed in all directions, around the graphene quantum dot supercell. Only the gamma point was taken into account in all of the DFT calculations for this study.

## 3. Results and discussion

### 3.1. Structural characterization of the doped catalysts

The doped mesoporous carbon nanostructures were prepared using an SBA-15 template with intended ratios of cysteine:Fe-TMPP = 2:0, 0:0.3, 2:0.3, and 2:1 (denoted as Cys2/Fe0/C, Cys0/Fe0.3/C, Cys2/Fe0.3/C, and Cys2/Fe1/C, respectively) (Fig. 1). The morphology and elemental distribution of the as-prepared samples were characterized using FE-TEM and EDX-mapping analysis. All the as-prepared samples exhibited a SBA-15 template-based porous structure, demonstrating the fairly effective transferring of the porous template to the carbon structure. As shown in Fig. 2(a), Cys2/Fe0/C synthesized with Fe-TMPP in the absence of cysteine exhibited a relatively unclear porous structure with low crystallinity. On the other hand, Cys0/Fe0.3/C prepared with Fe-TMPP in the absence of cysteine showed a relatively porous structure with fairly high crystallinity (Fig. 2(b)). Cys2/Fe0.3/C prepared with both Fe-TMPP and cysteine showed a uniformly arranged porous structure with a regularly formed cylindrical shape (Fig. 2(c)). However, compared to Cys2/Fe0.3/C, Cys2/Fe1/C prepared with an increased amount of Fe-TMPP contained Fe nanoparticles within the porous carbon structure due to an excessive amount of Fe-TMPP as a dopant (Fig. 2(d)). In particular, Cys0/Fe0.3/C, Cys2/Fe0.3/C, and Cys2/Fe1/C exhibited homogeneous elemental distribution in the carbon structure containing Fe phases acting as electrochemical active sites for ORR despite an acid treatment in the HF solution for 2 h.

Fig. 3(a) shows XRD patterns of Cys2/Fe0/C, Cys0/Fe0.3/C, Cys2/Fe0.3/C, and Cys2/Fe1/C. The XRD peaks at  $\sim 23^\circ$  and  $\sim 44^\circ$

corresponding to (002) and (110), respectively, in the carbon structures were negatively shifted, compared to  $\sim 26^\circ$  and  $\sim 43^\circ$  corresponding to (002) and (110), respectively, in a typical hexagonal graphitic structure [45]. The negative shift of the XRD peak patterns might be due to the doping effect of N and S. In particular, Cys2/Fe0/C and Cys2/Fe0.3/C containing sulfur as a dopant exhibited a more negative shift than Cys0/Fe0.3/C without sulfur, which might be attributed to the larger atomic size of sulfur than that of nitrogen [46]. Furthermore, the broad diffraction patterns of the samples could result from the doping effect of the heteroatoms [21,47,48]. Fig. 3(b) shows the Raman spectra of Cys2/Fe0/C, Cys0/Fe0.3/C, Cys2/Fe0.3/C, and Cys2/Fe1/C. In the Raman spectra, the characteristic peaks at  $1350\text{ cm}^{-1}$  of the D band and  $1594\text{ cm}^{-1}$  of the G band represent the disordered structure due to the doping effect and graphitic  $\text{sp}^2$  carbon structure, respectively. Thus, the relative intensity ratio, i.e.  $I_D/I_G$ , implies a degree of disorder in the carbon structure [49,50]. The values of  $I_D/I_G$  for Cys2/Fe0/C, Cys0/Fe0.3/C, Cys2/Fe0.3/C, and Cys2/Fe1/C were 1.06, 1.02, 1.08, and 1.04, respectively. Cys2/Fe0/C, Cys2/Fe0.3/C, and Cys2/Fe1/C prepared using cysteine exhibited relatively higher  $I_D/I_G$  values, compared to Cys0/Fe0.3/C due to the doping effect of S. Especially, sulfur as a dopant in cysteine could dominantly lead to the deformation of the carbon structure, as previously observed in the XRD data [21,48]. The specific surface area and pore size distribution of the samples are shown in Fig. 3(c) and (d). Cys2/Fe0/C exhibited an increased specific surface area of  $\sim 854\text{ m}^2\text{ g}^{-1}$  and an average pore size of  $\sim 3.81\text{ nm}$ , compared to the SBA-15 template ( $816\text{ m}^2\text{ g}^{-1}$ ), due to the formation of an open edge and high curvature in the S-doped carbon structure [21,48,50]. Cys0/Fe0.3/C exhibited a specific surface area of  $\sim 924\text{ m}^2\text{ g}^{-1}$  and an average pore size of  $\sim 3.65\text{ nm}$ . Furthermore, Cys2/Fe0.3/C prepared using both cysteine and Fe-TMPP exhibited the highest specific surface area of  $\sim 1027\text{ m}^2\text{ g}^{-1}$  and an average pore size of  $\sim 3.21\text{ nm}$ . On the other hand, Cys2/Fe1/C exhibited a low specific surface area of  $\sim 682\text{ m}^2\text{ g}^{-1}$  and a reduced micropore region in the isotherm, resulting from the formation of Fe nanoparticles due to a relative excess amount of Fe-TMPP.

The surface area and pore structure of the samples might be strongly dependent on a chemical interaction between cysteine and Fe-TMPP during synthesis. To investigate the interaction in the doped carbon structures, TGA was performed with cysteine, Fe-TMPP, and a mixture of SBA-15:cysteine:Fe-TMPP (1:2:0.3) in the temperature range of 30–900 °C under an  $\text{N}_2$  atmosphere (Fig. 4). The cysteine was decomposed at a relatively low temperature of 200 °C with a high weight loss of 95.4% up to 900 °C, whereas the Fe-TMPP showed a relatively low weight loss of 33.8% up to 900 °C. The mixture of SBA-

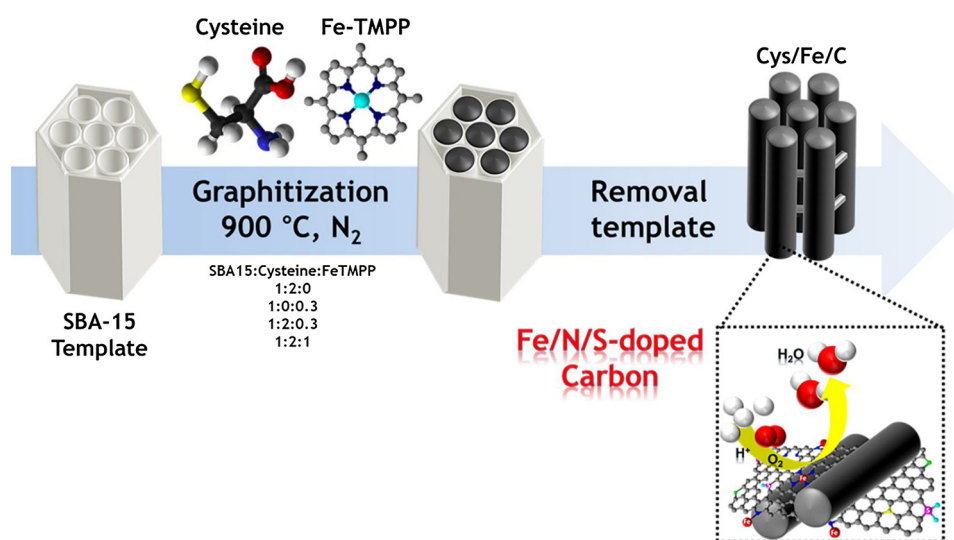


Fig. 1. Schematic illustration of synthesis of Fe/N/S-doped carbon nanostructures prepared using a template method.

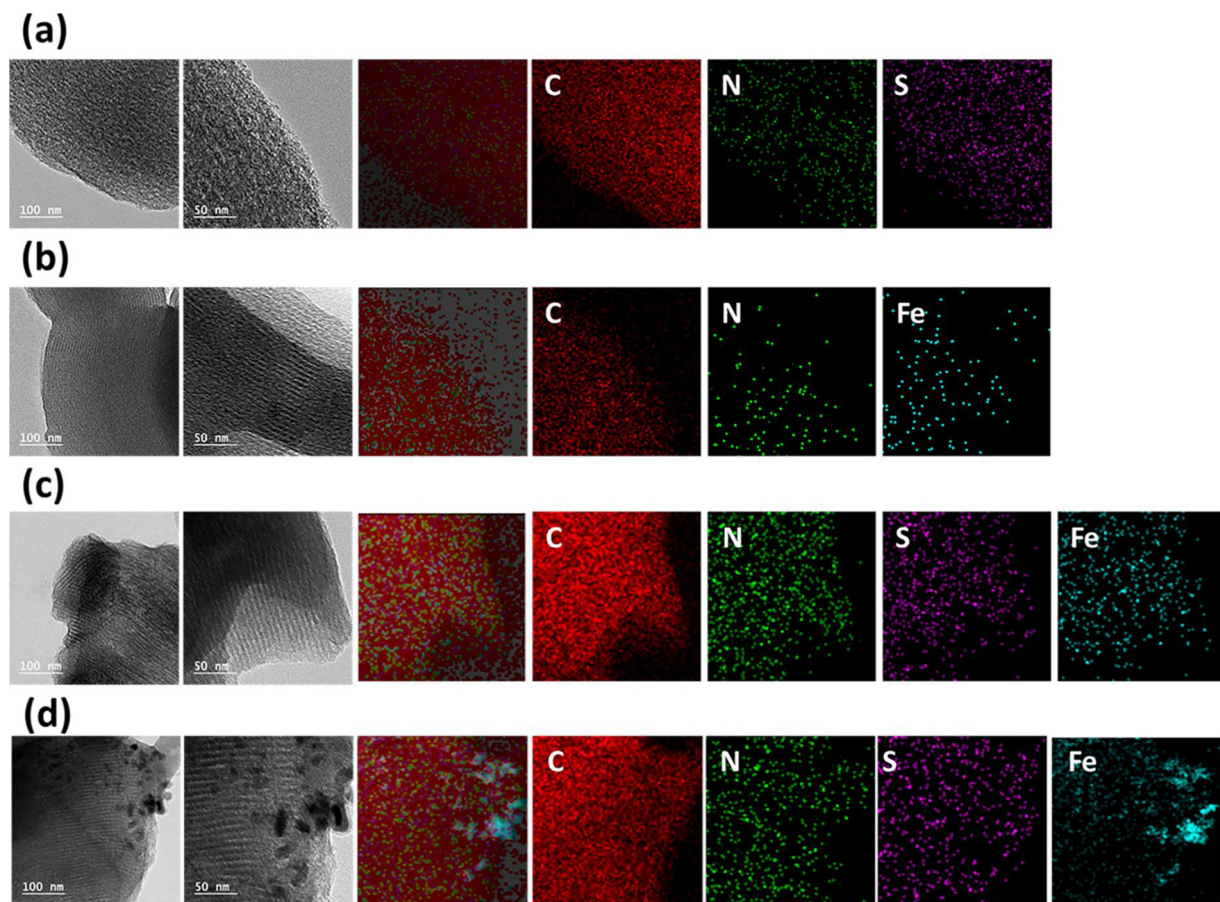


Fig. 2. STEM-EDX elemental mapping images of (a) Cys2/Fe0/C, (b) Cys0/Fe0.3/C, (c) Cys2/Fe0.3/C, and (d) Cys2/Fe1/C.

15:cysteine:Fe-TMPP(1:2:0.3) exhibited a significantly low weight loss of 41.6% up to 900 °C, compared to the cysteine in the absence of the Fe-TMPP. Furthermore, as indicated in the TGA curves in the DSC data (Figure S1), the Fe-TMPP showed the recrystallization process of the Fe-TMPP at > 300 °C with a slight weight loss up to 300 °C. On the other hand, the cysteine was fused and then recrystallized at 200 °C with a high weight loss of 95.4% up to 900 °C. The mixture of SBA-15:cysteine:Fe-TMPP(1:2:0.3) showed a relatively low weight loss, compared to the cysteine in the absence of the Fe-TMPP. This might result from the enhanced thermal stability of the mixture precursor due to the interaction between the fused cysteine and Fe-TMPP maintaining a macrocyclic structure. As a result, the mixed precursor for the synthesis of Cys2/Fe0.3/C can result in a stable carbonization process accompanied with the co-doping by sulfur and nitrogen from cysteine and Fe-TMPP and enhanced specific surface area.

The surface feature of the as-prepared samples was observed using FT-IR analysis (Figure S2). In the FT-IR spectra, Cys2/Fe0/C, Cys2/Fe0.3/C, and Cys2/Fe1/C showed the absorption bands at 3400, 2928, and 1600  $\text{cm}^{-1}$  corresponding to the vibrations of O—H/N—H, C—H, and C=C/C=O, respectively. In addition, the infrared (IR) bands at 1640 and 1443  $\text{cm}^{-1}$  correspond to the vibrations of C=N and C—N, respectively, reflecting nitrogen atoms in the carbon lattices. In particular, the IR band at 700  $\text{cm}^{-1}$  and 1190  $\text{cm}^{-1}$  corresponds to the vibration of the C—S bond in the samples, except for Cys0/Fe0.3/C [51–54]. The elemental contents and chemical states of the doped carbon structures were characterized using XPS analysis (Fig. 5). The amounts of nitrogen as a dopant were 5.57, 3.73, 4.52, and 2.93 at% for Cys2/Fe0/C, Cys0/Fe0.3/C, Cys2/Fe0.3/C, and Cys2/Fe1/C, respectively. The N1s spectra of the samples contained pyridinic (398.3–399.5 eV), pyrrolic (400.1–400.9 eV), graphitic (401.2–402.0 eV), and oxidized nitrogen states (403.4–410.0 eV). The

graphitic N is located at graphene plane or layer, substituting the carbon atom. Moreover, the pyridinic and pyrrolic N states are mainly combined with two carbon atoms, which are located at the edge or defect sites with ring types of hexagon and pentagon, respectively [32,55,56]. Especially, the pyridinic and pyrrolic N states are known as electrocatalytic active sites for ORR in the nitrogen functional group due to an increased density of electronic state in the doped carbon structures [57,58]. As shown in Fig. 5(e), Cys2/Fe0.3/C exhibited the highest portion of pyridinic and pyrrolic N states, which could be bound with Fe in the form of Fe-N<sub>x</sub> acting as a key active site for ORR. Thus, it is expected that Cys2/Fe0.3/C with a high portion of active sites could exhibit enhanced ORR performance. The amounts of iron in Cys0/Fe0.3/C and Cys2/Fe0.3/C were 0.24 and 0.29 at%, respectively (Figures S3(a) and S3(b), respectively). However, in the case of Cys2/Fe1/C, despite the synthesis with the Fe-TMPP, Fe was not detected due to the encapsulation of Fe nanoparticles by carbon layers (Figure S3(c)), as previously observed in the TEM image (Fig. 2(d)). From the S2p spectra of the samples, the amounts of sulfur were determined to be 0.84, 0.49, and 0.55 at% for Cys2/Fe0/C, Cys2/Fe0.3/C, and Cys2/Fe1/C, respectively (Figures S3(d), S3(e), and S3(f), respectively). The S2p spectra were fitted with C—S—C, C=S, and C—S(O)<sub>x</sub>—C at 163.9, 165.1, and 167.8 eV, respectively [16,59,60]. In particular, the thiophenic S (C—S—C) in the doped carbon catalysts is well known as an ORR active site [61,62]. In general, the doped sulfur in the doped carbon could be located with a form of the C—S bond in the edge or defect sites due to a similar electroneutrality to carbon [58,63]. The amounts of S and portions of the thiophenic S in the samples decreased with the addition of Fe-TMPP (Cys2/Fe0/C: 0.84 at%/84.71%, Cys2/Fe0.3/C: 0.49 at %/63.48%, Cys2/Fe1/C: 0.55 at%/49.73%, respectively) (Table 1) [64,65].

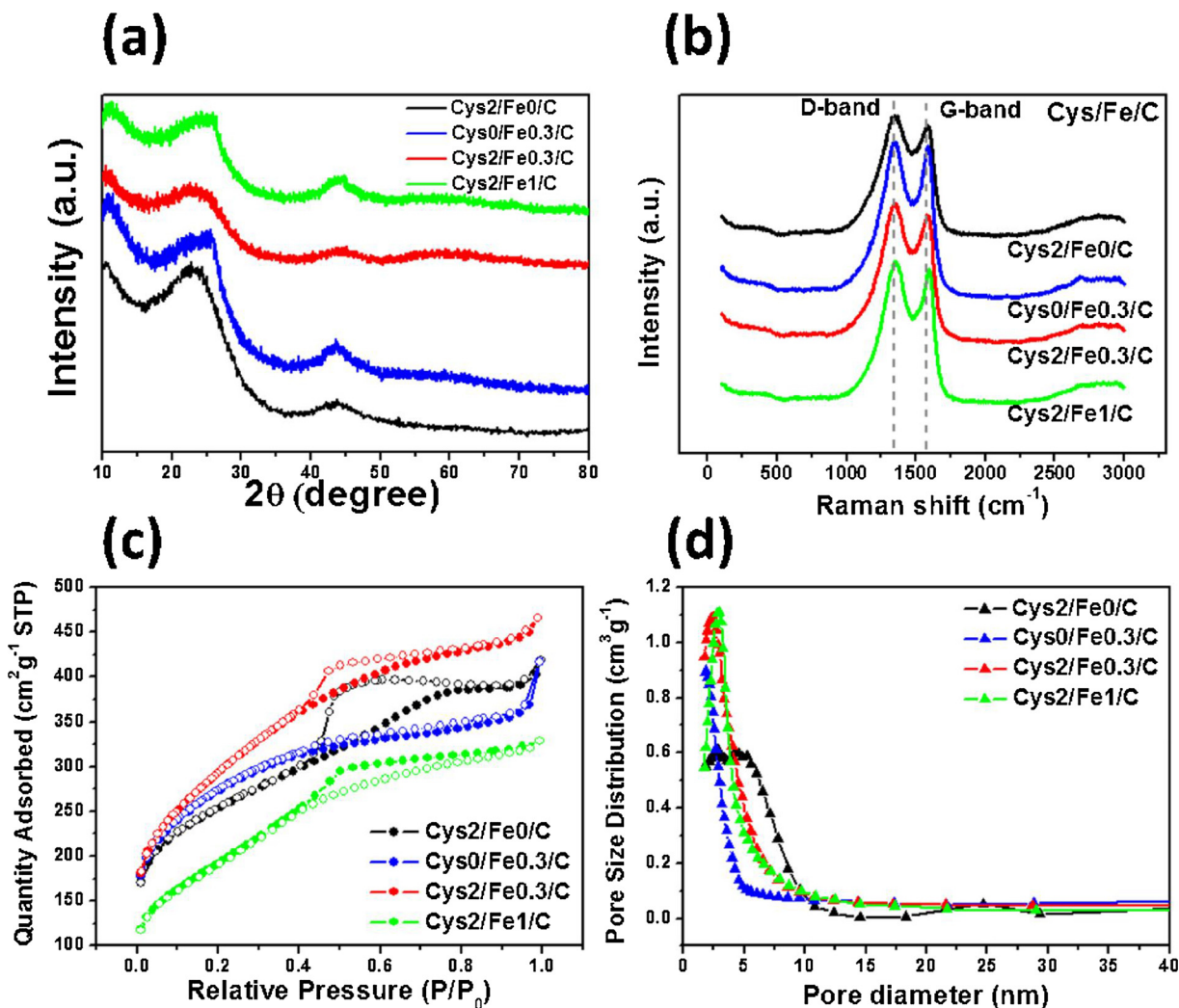


Fig. 3. (a) Wide angle XRD patterns, (b) Raman spectra, (c) nitrogen gas adsorption-desorption isotherms, and (d) pore size distributions of Cys2/Fe0/C, Cys0/Fe0.3/C, Cys2/Fe0.3/C, and Cys2/Fe1/C.

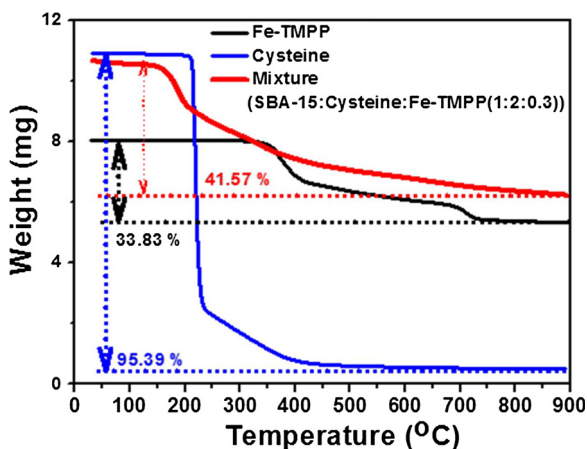


Fig. 4. TGA curves of Fe-TMPP, Cysteine, and mixture of SBA-15:Cysteine:Fe-TMPP(1:2:0.3).

### 3.2. Electrochemical properties of the doped catalysts

To characterize the electrochemical properties of the cathode catalysts for ORR in an acid medium, CVs for Cys2/Fe0/C, Cys0/Fe0.3/C, Cys2/Fe0.3/C, and Cys2/Fe1/C were obtained in Ar and O<sub>2</sub>-saturated

0.5 M H<sub>2</sub>SO<sub>4</sub>, as shown in Figures S4(a), S4(b), S4(c), and S4(d), respectively. The ORR peak potentials for Cys2/Fe0/C, Cys0/Fe0.3/C, Cys2/Fe0.3/C, and Cys2/Fe1/C were 0.27 V, 0.75 V, 0.76 V, and 0.74 V, respectively. Compared to Cys2/Fe0/C and Cys0/Fe0.3/C, Cys2/Fe0.3/C exhibited the highest peak potential for ORR, resulting from the reduced over-potential for ORR by the synergistic effect between the co-doping of N/S and mesoporous nanostructure [36]. To further evaluate the electrocatalytic activity of the catalysts for ORR in an acid medium, LSVs for Cys2/Fe0/C, Cys0/Fe0.3/C, Cys2/Fe0.3/C, and Cys2/Fe1/C were obtained in O<sub>2</sub>-saturated 0.5 M H<sub>2</sub>SO<sub>4</sub>, as shown in Figures S4(e), S4(f), S4(g), and S4(h), respectively. All the catalysts exhibited typical characteristic polarization curves for ORR with activation, ohmic, and mass transport losses at different rotating speeds. The LSVs were obtained in O<sub>2</sub>-saturated 0.5 M H<sub>2</sub>SO<sub>4</sub> using a rotating ring disk electrode (RRDE) at 1600 rpm. The disk (I<sub>D</sub>) and ring (I<sub>R</sub>) currents represent the specific values produced during the main ORR process and generated by the side reaction for a by-product, respectively (Fig. 6(a)) [66,67]. The specific current densities (I<sub>D</sub>) for Cys2/Fe0/C, Cys0/Fe0.3/C, and Cys2/Fe0.3/C, and Pt/C measured at 0.9 V were 0.13, 0.31, 0.84, and 0.37 mA cm<sup>-2</sup>, respectively. The half-wave potentials (E<sub>1/2</sub>) for Cys2/Fe0/C, Cys0/Fe0.3/C, Cys2/Fe0.3/C, and Pt/C were 0.46, 0.82, 0.86, and 0.84 V, respectively. Cys2/Fe0.3/C showed a significantly improved ORR activity, i.e. high I<sub>D</sub> and high E<sub>1/2</sub>, even compared to a commercial Pt/C catalyst. The electron-transfer number (n) and generation rate of hydrogen peroxide (%H<sub>2</sub>O<sub>2</sub>) of the catalysts

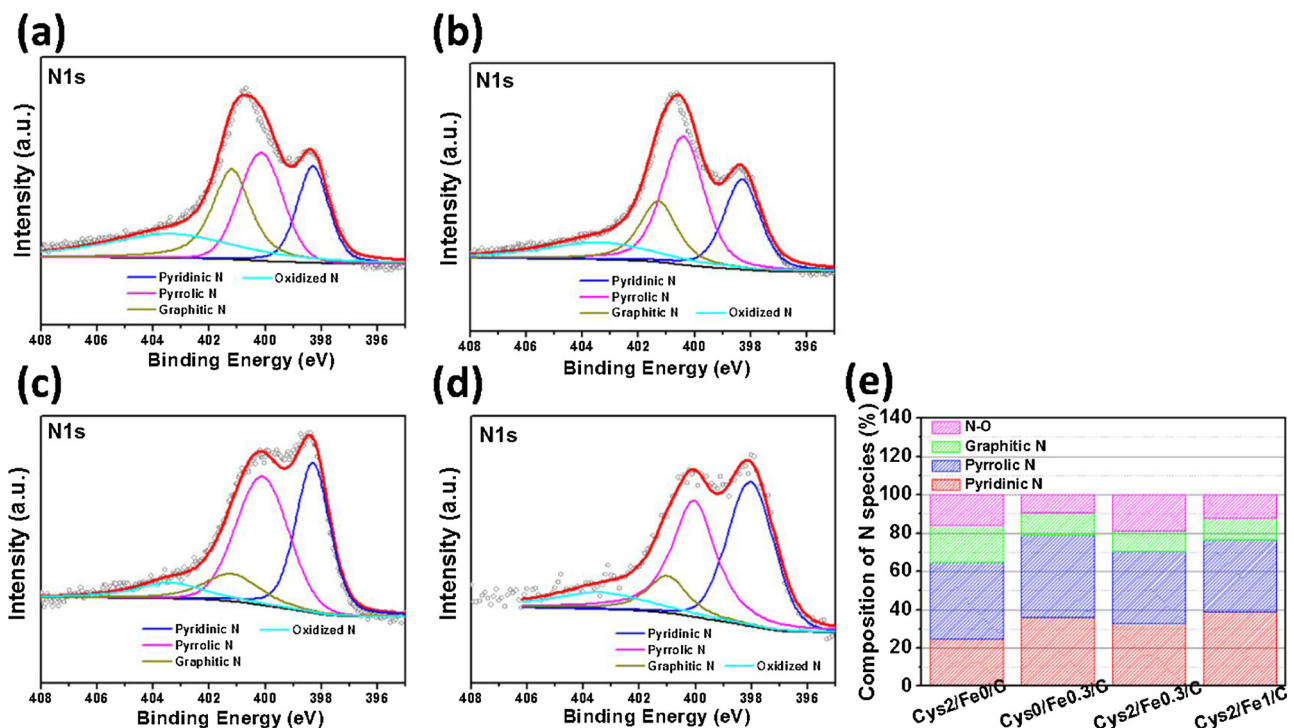


Fig. 5. XPS N1s spectra of (a) Cys2/Fe0/C, (b) Cys0/Fe0.3/C, (c) Cys2/Fe0.3/C, and (d) Cys2/Fe1C. (e) Comparison of nitrogen species in the as-prepared carbon nanostructures.

Table 1

BET surface area, surface N, S, and Fe content, and ORR performance of the obtained catalysts.

	Cys2/Fe0/C	Cys0/Fe0.3/C	Cys2/Fe0.3/C	Cys2/Fe1C
BET surface area (m <sup>2</sup> /g)	853.53	924.05	1027.03	681.97
Surface N content (at %)	5.57	3.73	4.52	2.93
Pyridinic N + Pyrrolic N (%)	64.77	70.46	78.87	76.64
Surface Fe content (at %)	–	0.24	0.29	Not detected
Surface S content (at %)	0.84	–	0.49	0.55
Thio-phenic S (%)	84.71	–	63.48	49.73
Specific activity (mA cm <sup>-2</sup> ) at 0.9V	0.13	0.31	0.83	0.63
Half-wave potential (V)	0.46	0.82	0.86	0.85

during the ORR process are determined using Eq. (1) and Eq. (2).

$$n = \frac{4I_D}{I_D + I_R/N} \quad (1)$$

$$\%H_2O_2 = \frac{200I_R}{I_DN + I_R} \quad (2)$$

where  $I_D$  and  $I_R$  are the values measured on carbon rotating and Pt ring-disk electrodes, respectively, and  $N$  is the collecting coefficient number (-0.4245 for this equipment) [68]. In particular, Cys2/Fe0.3/C exhibited a complete electron-transfer number approaching 4 with low %  $H_2O_2$  as shown in Fig. 6(c). Compared to Cys0/Fe0.3/C, Cys2/Fe0.3/C showed improved ORR performance due to the synergistic effect of the co-doping of N/S and high specific surface area. The ORR activity of Cys2/Fe0.3/C (prepared with cysteine and an appropriate amount of Fe-TMPP) was significantly superior to that of Cys2/Fe0/C and Cys2/Fe1/C (prepared with cysteine in the absence of Fe-TMPP and with cysteine and an excessive amount of Fe-TMPP, respectively) (Figure S5). As a result, the improved ORR activity of Cys2/Fe0.3/C, compared to a commercial Pt/C, might be attributed to a mesoporous structure with a large specific surface area and high portion of electrocatalytic

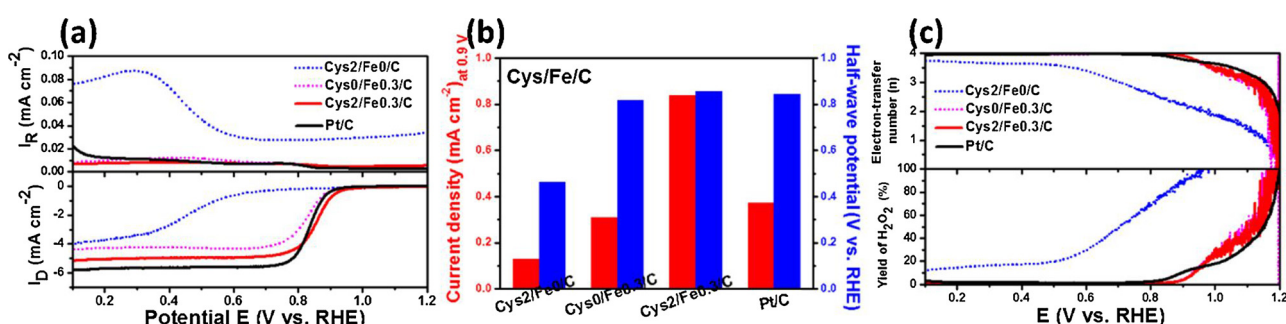


Fig. 6. (a) RRDE polarization curves of Cys2/Fe0/C, Cys0/Fe0.3/C, Cys2/Fe0.3/C, and Pt/C. in  $O_2$ -saturated 0.5 M  $H_2SO_4$  with a scan rate of 1 mV s<sup>-1</sup> and an electrode rotation rate of 1600 rpm at room temperature. The ring potential was maintained at 1.15 V vs. Ag/AgCl. (b) Comparison of specific activity at 0.9 V (vs. RHE) and half-wave potentials for the samples. (c) Plots of the electron-transfer number (n) and generation yield of hydrogen peroxide (% $H_2O_2$ ) during the ORR.

active sites doped by heteroatoms (Table 1). To evaluate the durability of the cathode catalysts for ORR, a stability test was performed by 10,000 cycles in the potential range of 0.7–1.2 V (Figure S6). From the LSVs for the catalysts before and after the stability test, the difference of  $E_{1/2}$  before and after the stability test ( $\Delta E_{1/2}$ ) were compared as shown in Figure S6. The values of  $\Delta E_{1/2}$  for Cys2/Fe0/C, Cys0/Fe0.3/C, Cys2/Fe0.3/C, Cys2/Fe1/C, and Pt/C were 31, 73, 32, 60, and 80 mV, respectively, exhibiting the significantly improved stability of Cys2/Fe0.3/C for ORR. Furthermore, the morphology and structure of Cys2/Fe0.3/C were characterized using TEM and EDX mapping analysis before and after the stability test (Figure S7). Cys2/Fe0.3/C maintained the doped mesoporous structure without serious destruction with the slight reduction of dopants.

To confirm the effect of iron species in the doped catalysts on ORR,  $\text{CN}^-$  ion poisoning analysis for Cys2/Fe0/C, Cys0/Fe0.3/C, Cys2/Fe0.3/C, and Cys2/Fe1/C was carried out by comparing the LSVs in  $\text{O}_2$ -saturated 0.5 M  $\text{H}_2\text{SO}_4$  with and without 10 mM KCN. Yeager et al. investigated the effect of the oxygen reduction process in Co/Fe-doped catalysts in the presence of  $\text{CN}^-$  ion and observed the decreased ORR activity [69]. Also, Thorum et al. reported the deteriorated ORR performance of iron phthalocyanine due to the decreased active sites by the  $\text{CN}^-$ -adsorption of the Fe-related species Cys2/Fe0/C prepared in the absence of Fe-TMPP, showing almost no difference in the LSVs for ORR between the absence and presence of KCN (Figure S7(a)) [70,71]. However, Cys0/Fe0.3/C, Cys2/Fe0.3/C, and Cys2/Fe1/C containing iron species exhibited the difference of half-wave potentials between the absence and presence of KCN of 21, 31, and 36 mV, respectively, for ORR, demonstrating the deteriorated ORR activity due to the preferable adsorption of  $\text{CN}^-$  ion on the Fe-doped catalysts [72]. Thus, it can be concluded that the iron species in the doped catalysts might act as a significant electrocatalytic active site for ORR.

### 3.3. DFT calculation of the doped catalyst

The Fe/N/S-doped carbon nanostructures with electrocatalytic active sites, such as thiophenic S (pyrrole), thiophenic S (pyridine), thiophenic S-pyridinic N, and undoped carbon, as NPM cathode catalysts showed superior ORR performance to that of a commercial Pt/C catalyst, as previously reported in the literature and in our study [18,32]. In particular, the ORR activity can be determined by the parameter of the bond strength between the surface sites and the ORR chemical species ( $\text{O}_2$ , H, O, OH, OOH, HOOH, and  $\text{H}_2\text{O}$ ). In this study, among the ORR chemical species, the adsorption energy ( $\Delta G_{\text{ad}}$ ) of oxygen molecules on the active sites in the Fe/S/N-doped carbon nanostructures could be determined by DFT calculation [33,73–76]:

$$\Delta G_{\text{ad}} = E_{\text{substr}-\text{O}_2} - E_{\text{substr}} - \mu_{\text{O}_2} \quad (3)$$

where  $\Delta G_{\text{ad}}$ ,  $E_{\text{substr}-\text{O}_2}$ , and  $E_{\text{substr}}$  are the adsorption free energy, the total energies of  $\text{O}_2$ -adsorbed, and the clean carbon substrates, respectively, and  $\mu_{\text{O}_2}$  is the chemical potential of  $\text{O}_2$ . The  $\mu_{\text{O}_2}$  can be expressed as a function of temperature and partial pressure of  $\text{O}_2$  as follows [77]:

$$\mu_{\text{O}_2} = \mu_{\text{O}_2(\text{standard})} + k_B T \ln(P_{\text{O}_2}/P_{\text{O}_2}^\circ) \quad (4)$$

where  $\mu_{\text{O}_2}$ ,  $\mu_{\text{O}_2(\text{standard})}$ ,  $k_B$ , T,  $P_{\text{O}_2}$ , and  $P_{\text{O}_2}^\circ$  are chemical potential, chemical potential at standard temperature and pressure, Boltzmann constant, temperature, partial pressure of oxygen, and partial pressure of oxygen under a standard condition, respectively. The adsorption energies of  $\text{O}_2$  molecule in the thiophenic S (pyrrole), thiophenic S (pyridine), the co-doping site between pyridinic N and thiophenic S, and the undoped carbon structure were calculated and compared as shown in Figure 7 and Table 2. The thiophenic S (pyrrole) and thiophenic S (pyridine) in the carbon structures without the N-doped site exhibited  $\text{O}_2$ -adsorption energies of 0.3 and -0.28 eV, respectively, representing the relatively weak adsorption of the  $\text{O}_2$  molecule, i.e. unfavorable ORR

process. However, the co-doping of thiophenic S and pyridinic N in the carbon matrix significantly increased the adsorption energy of the  $\text{O}_2$  molecule (-3.51 eV), compared to pure thiophenic S (-0.28 eV) and pyridinic N (-0.68 eV) leading to the favorable ORR.

### 3.4. Electrochemical performance of the doped catalysts

Fig. 8 shows the polarization curves of the PEMFCs measured using Cys2/Fe0/C, Cys0/Fe0.3/C, and Cys2/Fe0.3/C as the cathode catalysts at 80 °C under an ambient pressure. The maximal power densities for Cys2/Fe0/C, Cys0/Fe0.3/C, and Cys2/Fe0.3/C were 117, 299, and 349 mW  $\text{cm}^{-2}$ , respectively. Moreover, the current densities measured at 0.6 V for Cys2/Fe0/C, Cys0/Fe0.3/C, and Cys2/Fe0.3/C were 100, 210, and 267 mA  $\text{cm}^{-2}$ , respectively. The order of the PEMFC performance was Cys2/Fe0/C < Cys0/Fe0.3/C < Cys2/Fe0.3/C, which is in agreement with the electrochemical data for ORR from the half-cell measurement (Fig. 6). The PEMFC performance measured using the NPM catalysts was still lower than that of the Pt-based alloy cathode catalysts. However, according to the relevant recent reports, the  $\text{H}_2/\text{O}_2$  PEMFC measured using the NPM catalysts exhibited significantly improved performance of 700–900 mW  $\text{cm}^{-2}$  under back pressures of 0.5–2.0 bar [78–80]. Thus, to enhance the performance of PEMFCs fabricated with the NPM cathode catalyst, more efficient pore structures with high specific surface areas and increased doping sites and an optimization of the MEA structure, the fabrication process, and back pressure condition are needed.

### 3.5. Methanol tolerance of the doped catalyst

In direct methanol fuel cells (DMFCs), the crossover of methanol as a fuel can deteriorate the performance of Pt-based catalysts at the cathode due to the poisoning effect by methanol. On the other hand, it is known that the NPM cathode catalysts exhibit tolerance of methanol without mixed potentials by methanol oxidation reaction (MOR). To investigate the methanol tolerance of the cathode catalysts, LSVs for the catalysts were measured in  $\text{O}_2$ -saturated  $\text{H}_2\text{SO}_4$  solution containing different concentrations of methanol at a rotating speed of 1600 rpm. In the case of Pt/C, the oxidation peaks evidently appeared despite under the reduction potential for ORR (Fig. 9(a)). The oxidation current densities increased with increasing concentration of MeOH. These results indicated the significantly deteriorated ORR activity due to the mixed potential resulting from the oxidation of MeOH on Pt/C as a cathode catalyst. On the other hand, Cys2/Fe0.3/C as NPM catalysts exhibited no serious variation in the LSVs with increasing MeOH concentration in the  $\text{O}_2$ -saturated  $\text{H}_2\text{SO}_4$  solution (Fig. 9(b)), demonstrating the maintained ORR activity even in the presence of MeOH due to the tolerance of the NPM catalyst to MeOH. The variations of  $E_{1/2}$  of the cathode catalysts were expressed as a function of MeOH concentration in  $\text{O}_2$ -saturated  $\text{H}_2\text{SO}_4$  solution (Fig. 9(c)). Consequently, the tolerance and inactivity of the cross-over methanol for the NPM cathode catalysts can be suitable for their practical application to DMFCs. Table 3 shows a comparison of the structural properties and ORR performance of the state-of-the-art NPM catalysts [16,21,32,53,65,81–83]. In particular, compared to the NPM catalysts, Cys2/Fe0.3/C prepared using a template method with cysteine and Fe-TMPP as doping and carbon sources showed significantly superior ORR activity even in an acid medium. The enhanced ORR performance of Cys2/Fe0.3/C can be attributed to a relatively high specific surface area, well-defined porous structure, and electrochemical active sites by nitrogen, sulfur, and Fe-N<sub>x</sub>. Consequently, the NPM catalyst was synthesized via a green approach using a nontoxic, eco-friendly amino acid, cysteine, containing C, N, and S, exhibiting the ORR performance comparable even to a commercial Pt/C catalyst.

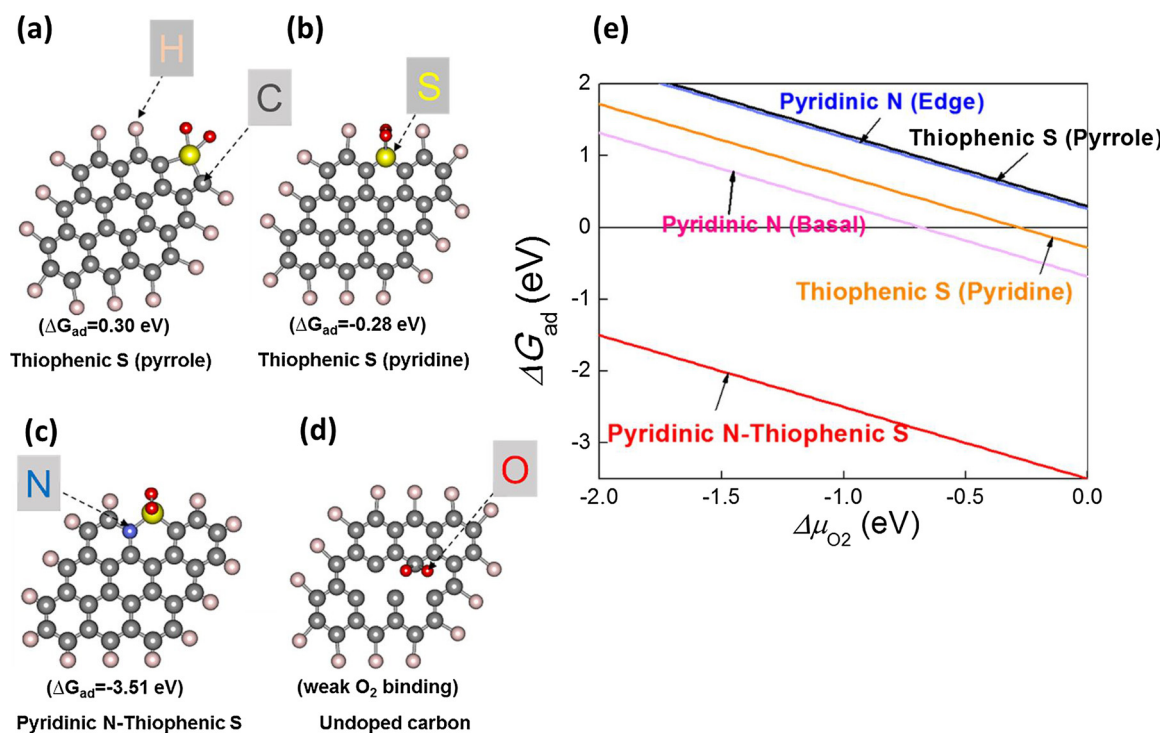


**Fig. 7.**  $O_2$  adsorption energy on surface and atomic structures of (a) thiophenic S (pyrrole), (b) thiophenic S (pyridine), (c) pyridinic N-thiophenic S, and (d) undoped carbon structure. The gray, pink, yellow, blue, and red balls represent the C, H, S, N, and O atoms, respectively. (e) Adsorption energy ( $\Delta G_{ad}$ ) of  $O_2$  on the active sites in the N/S-C calculated using the DFT (For interpretation of the references to colour in this figure legend, the reader is referred to the web version of this article).

**Table 2**

Adsorption energy ( $\Delta G_{ad}$ ) of  $O_2$  on the active sites in the N/S-C calculated using the DFT.

$\Delta G_{ad}$ at $\Delta \mu = 0$ (eV)
Thiophenic S (pyrrole)
Thiophenic S (pyridine)
Pyridinic N-Thiophenic S
Undoped carbon structure
Pyridinic N

#### 4. Conclusions

In this study, the NPM catalysts for ORR in an acid medium were synthesized using a template method with a nontoxic, eco-friendly cysteine containing C, N, and S and Fe-TMPP used as carbon and doping sources. In particular, Cys2/Fe0.3/C synthesized with an appropriate

ratio of cysteine and Fe-TMPP showed a relatively high specific surface area and fairly high portion of doped species (pyridinic and pyrrolic N, thiophenic S, and Fe- $N_x$ ). Compared to the commercial Pt/C cathode catalyst, Cys2/Fe0.3/C exhibited significantly superior ORR activity and stability in 0.5 M  $H_2SO_4$ , i.e. high half-wave potential, high specific activity, electron transfer number approaching 4, and slight difference between/after the stability test. Moreover, Cys2/Fe0.3/C exhibited superior methanol tolerance in 0.5 M  $H_2SO_4$  in the presence of MeOH. The improved ORR performance of Cys2/Fe0.3/C in an acid medium can be predominantly attributed to the synergistic effect between the co-doping of N, S, and Fe and the porous structure with a high specific surface area.

#### Acknowledgments

This research was supported by Basic Science Research Program through the National Research Foundation of Korea (NRF) funded by

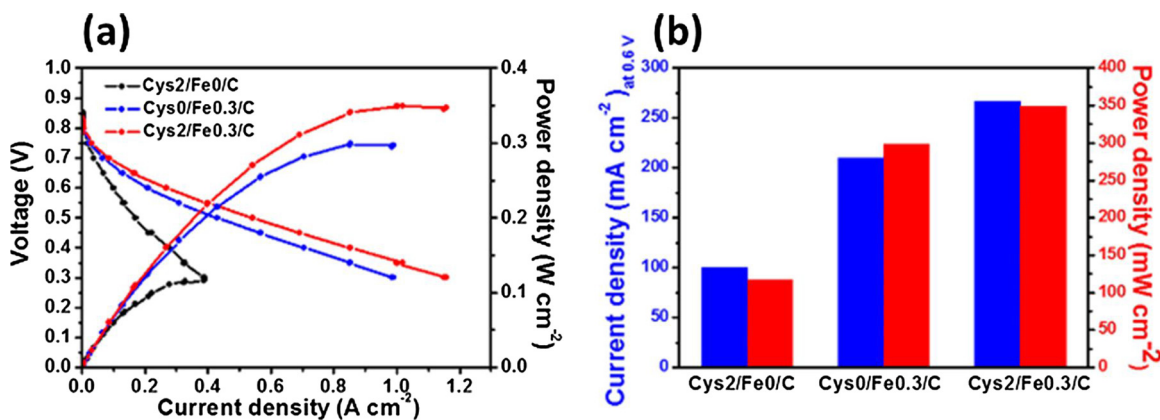


**Fig. 8.** (a) Polarization and power density plots of  $H_2$ - $O_2$  PEMFCs with Cys2/Fe0/C, Cys0/Fe0.3/C, and Cys2/Fe0.3/C as cathode catalysts at 80 °C. (b) Comparison of ORR activity for the as-prepared catalysts.

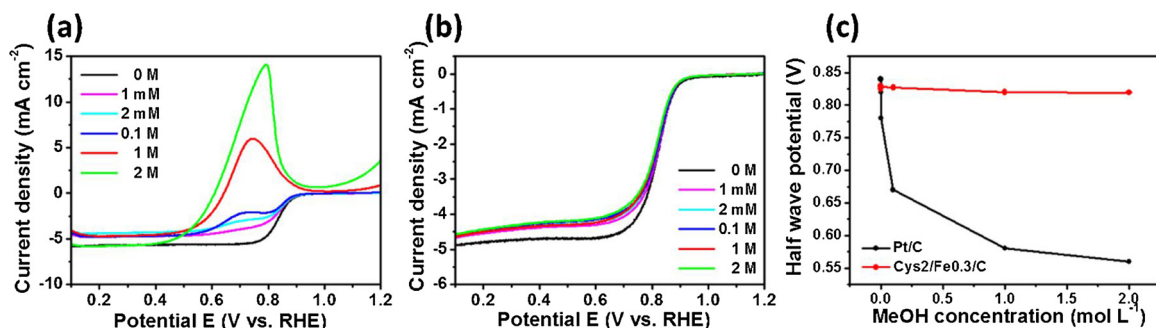


**Fig. 9.** (a) LSVs of Pt/C for ORR measured in O<sub>2</sub>-saturated 0.5 M H<sub>2</sub>SO<sub>4</sub> with different methanol concentrations at 25 °C. LSVs of (c) Cys2/Fe/0.3/C for ORR measured in O<sub>2</sub>-saturated 0.5 M H<sub>2</sub>SO<sub>4</sub> with different methanol concentrations at 25 °C. (c) Comparison of half-wave potentials of Pt/C and Cys2/Fe0.3/C measured in O<sub>2</sub>-saturated 0.5 M H<sub>2</sub>SO<sub>4</sub> containing different concentrations of MeOH.

**Table 3**  
Comparison of structural properties and ORR performance of the-state-of-the-art NPM catalysts.

Sample [ref.]	Pre-cursor (C, N, S)	Metal	BET surface area (m <sup>2</sup> /g)	Surface N content (at%)	Surface Fe content (at%)	Surface S content (at%)	Electrolyte	Onset potential (V)
Cys2/Fe0.3/C CA-TC,900 [63]	Cysteine S-(2-thienyl)-L cysteine	Fe-TMPP	1027.03	4.52	0.29	0.49	0.5 M H <sub>2</sub> SO <sub>4</sub>	0.95
PAA-CYS [21]	Cysteine	–	–	2.69	–	2.74	0.1 M HClO <sub>4</sub>	0.2 (Ag/AgCl)
SNCT-900-1/1 [76]	Cysteine	–	562	2.75	–	0.18	0.5 M H <sub>2</sub> SO <sub>4</sub>	0.851
(Fe <sub>1-x</sub> S/N, S-MGCS) 0.2 [16]	Dopamine, thiourea	FeSO <sub>4</sub>	401	1.94–2.05	0.82	3.05–3.20	0.1 M HClO <sub>4</sub>	0.81
Fe/N/C-SCN [77]	poly-mphenylenediamine (PmPDA), (NH <sub>4</sub> ) <sub>2</sub> S <sub>2</sub> O <sub>8</sub>	Fe (SCN) <sub>3</sub>	751	4.4	1.4	2.1	0.1 M HClO <sub>4</sub>	0.836 (Half-wave potential (V))
PF-1000 [78]	Ethylene-dioxy-thiophene	FeCl <sub>3</sub> ·6H <sub>2</sub> O	800	12.5	0.25	1.77	0.5 M H <sub>2</sub> SO <sub>4</sub>	0.89
Fe/N/S-MC (1:1:1) [32]	FeTMPP, thioacetamide	Fe-TMPP	1064.6	4.57	0.42	3.96	0.5 M H <sub>2</sub> SO <sub>4</sub>	0.89

the Ministry of Education (NRF-2016R1A2B2016033) and the Technology Development Program to Solve Climate Changes of the NRF funded by the Ministry of Science, ICT, (NRF-2017M1A2A2086648).

#### Appendix A. Supplementary data

Supplementary material related to this article can be found, in the online version, at doi:<https://doi.org/10.1016/j.apcatb.2018.07.013>.

#### References

- C.W.B. Bezerra, L. Zhang, K. Lee, H. Liu, A.L.B. Marques, E.P. Marques, H. Wang, J. Zhang, A review of Fe-N/C and Co-N/C catalysts for the oxygen reduction reaction, *Electrochim. Acta* 53 (2008) 4937–4951.
- V.R. Stamenkovic, B.S. Mun, M. Arenz, K.J.J. Mayrhofer, C.A. Lucas, G. Wang, P.N. Ross, N.M. Markovic, Trends in electrocatalysis on extended and nanoscale Pt-bimetallic alloy surfaces, *Nat. Mater.* 6 (2007) 241–247.
- M. Kaukonen, A.V. Krasheninnikov, E. Kauppinen, R.M. Nieminen, Doped graphene as a material for oxygen reduction reaction in hydrogen fuel cells: a computational study, *ACS Catal.* 3 (2013) 159–165.
- R. Bashyam, P. Zelenay, A class of non-precious metal composite catalysts for fuel cells, *Nature* 443 (2006) 63–66.
- H. Liu, Q. Yu, H. Fu, Y. Wan, X. Qu, Z. Xu, D. Yin, S. Zheng, Pt supported on ordered microporous carbon as highly active catalyst for catalytic hydrodeiodination of iodinated X-ray contrast media, *Appl. Catal. B* 222 (2018) 167–175.
- Y. Jiao, Y. Zheng, M. Jaroniec, S.Z. Qiao, E. Measurements, Origin of the electrocatalytic oxygen reduction activity of graphene-based catalysts: a roadmap to achieve the best performance, *J. Am. Chem. Soc.* 136 (2014) 4394–4403.
- M. Li, L. Zhang, Q. Xu, J. Niu, Z. Xia, N-doped graphene as catalysts for oxygen reduction and oxygen evolution reactions: theoretical considerations, *J. Catal.* 314 (2014) 66–72.
- S. Yuan, J.L. Shui, L. Grabstanowicz, C. Chen, S. Commet, B. Reprogne, T. Xu, L. Yu, D.J. Liu, A highly active and support-free oxygen reduction catalyst prepared from ultrahigh-surface-area porous polyporphyrin, *Angew. Chem. Int. Ed.* 52 (2013) 8349–8353.
- J. Greeley, I.E.L. Stephens, A.S. Bondarenko, T.P. Johansson, H.A. Hansen, T.F. Jaramillo, J. Rossmeisl, I. Chorkendorff, J.K. Nørskov, Alloys of platinum and early transition metals as oxygen reduction electrocatalysts, *Nat. Chem.* 1 (2009) 552–556.
- K. Mamani, D. Jain, D. Dogu, V. Gustin, S. Gunduz, A.C. Co, U.S. Ozkan, Insights into oxygen reduction reaction (ORR) and oxygen evolution reaction (OER) active sites for nitrogen-doped carbon nanostructures (CN<sub>x</sub>) in acidic media, *Appl. Catal. B* 220 (2018) 88–97.
- L. Dai, Y. Xue, L. Qu, H.-J. Choi, J.-B. Baek, Metal-free catalysts for oxygen reduction reaction, *Chem. Rev.* 115 (2015) 4823–4892.
- X. Liu, L. Dai, Carbon-based metal-free catalysts, *Nat. Rev. Mater.* 1 (2016) 1–13.
- G. Wu, P. Zelenay, Nanostructured nonprecious metal catalysts for oxygen reduction reaction, *Acc. Chem. Res.* 46 (2013) 1878–1889.
- A. Morozan, B. Joussetme, S. Palacin, Low-platinum and platinum-free catalysts for the oxygen reduction reaction at fuel cell cathodes, *Energy Environ. Sci.* 4 (2011) 1238–1254.
- L.D. Liangti Qu, Yong Liu, Jong-Beom Baek, Nitrogen-doped graphene as efficient metal-free electrocatalyst for oxygen reduction in fuel cells, *ACS Nano* 3 (2010) 1321–1326.
- J. Xiao, Y. Xia, C. Hu, J. Xi, S. Wang, Raisin bread-like iron sulfides/nitrogen and

sulfur dual-doped mesoporous graphitic carbon spheres: a promising electrocatalyst for the oxygen reduction reaction in alkaline and acidic media, *J. Mater. Chem. A* 5 (2017) 11114–11123.

[17] X. Liu, W. Zhou, L. Yang, L. Li, Z. Zhang, Y. Ke, S. Chen, Nitrogen and sulfur co-doped porous carbon derived from human hair as highly efficient metal-free electrocatalysts for hydrogen evolution reactions, *J. Mater. Chem. A* 3 (2015) 8840–8846.

[18] H.-S. Park, S.-B. Han, D.-H. Kwak, G.-H. Lee, I.-A. Choi, D.-H. Kim, K.-B. Ma, M.-C. Kim, H.-J. Kwon, K.-W. Park, Sulfur-doped porphyrinic carbon nanostructures synthesized by amorphous MoS 2 for the oxygen reduction reaction in an acidic medium, *ChemSusChem* 10 (2017) 2202–2209.

[19] S. Li, W. Xu, P. Cheng, J. Luo, D. Zhou, J. Li, R. Li, D. Yuan, Bacterial cellulose derived iron and phosphorus co-doped carbon nanofibers as an efficient oxygen reduction reaction electrocatalysts, *Synth. Met.* 223 (2017) 137–144.

[20] M. Borghei, N. Laocharoen, E. Kibena-Pöldsepp, L.S. Johansson, J. Campbell, E. Kauppinen, K. Tammeveski, O.J. Rojas, Porous N,P-doped carbon from coconut shells with high electrocatalytic activity for oxygen reduction: alternative to Pt-C for alkaline fuel cells, *Appl. Catal. B Environ.* 204 (2017) 394–402.

[21] C.H. Choi, S.H. Park, S.I. Woo, Heteroatom doped carbons prepared by the pyrolysis of bio-derived amino acids as highly active catalysts for oxygen electro-reduction reactions, *Green Chem.* 13 (2011) 406–412.

[22] M. Liu, R. Zhang, W. Chen, Graphene-supported nanoelectrocatalysts for fuel cells: synthesis, properties, and applications, *Chem. Rev.* 114 (2014) 5117–5160.

[23] W. Zhou, J. Jia, J. Lu, L. Yang, D. Hou, G. Li, S. Chen, Recent developments of carbon-based electrocatalysts for hydrogen evolution reaction, *Nano Energy* 28 (2016) 29–43.

[24] Z.-J. Jiang, Z. Jiang, Reduction of the oxygen reduction reaction overpotential of nitrogen-doped graphene by designing it to a microspherical hollow shape, *J. Mater. Chem. A* 2 (2014) 14071–14081.

[25] J. Yan, H. Meng, F. Xie, X. Yuan, W. Yu, W. Lin, W. Ouyang, D. Yuan, Metal free nitrogen doped hollow mesoporous graphene-analogous spheres as effective electrocatalyst for oxygen reduction reaction, *J. Power Sources* 245 (2014) 772–778.

[26] B. Lu, T.J. Smart, D. Qin, J.E. Lu, N. Wang, L. Chen, Y. Peng, Y. Ping, S. Chen, Nitrogen and iron-codoped carbon hollow nanotubules as high-performance catalysts toward oxygen reduction reaction: a combined experimental and theoretical study, *Chem. Mater.* 29 (2017) 5617–5628.

[27] S.M. Unni, S. Devulapally, N. Karjule, S. Kurungot, Graphene enriched with pyrrolic coordination of the doped nitrogen as an efficient metal-free electrocatalyst for oxygen reduction, *J. Mater. Chem.* 22 (2012) 23506–23513.

[28] D. Shin, B. Jeong, B.S. Mun, H. Jeon, H.J. Shin, J. Baik, J. Lee, On the origin of electrocatalytic oxygen reduction reaction on electrospun nitrogen – carbon species, *J. Phys. Chem. C* 117 (2013) 11619–11624.

[29] C. Zhang, R. Hao, H. Liao, Y. Hou, Synthesis of amino-functionalized graphene as metal-free catalyst and exploration of the roles of various nitrogen states in oxygen reduction reaction, *Nano Energy* 2 (2013) 88–97.

[30] T. Wu, H. Shen, L. Sun, B. Cheng, B. Liu, J. Shen, Nitrogen and boron doped monolayer graphene by chemical vapor deposition using polystyrene, urea and boric acid, *New J. Chem.* 36 (2012) 1385–1391.

[31] H. Zhang, X. Liu, G. He, X. Zhang, S. Bao, W. Hu, Bioinspired synthesis of nitrogen/sulfur co-doped graphene as an efficient electrocatalyst for oxygen reduction reaction, *J. Power Sources* 279 (2015) 252–258.

[32] D.-H. Kwak, S.-B. Han, Y.-W. Lee, H.-S. Park, I.-A. Choi, K.-B. Ma, M.-C. Kim, S.-J. Kim, D.-H. Kim, J.-I. Sohn, K.-W. Park, Fe/N/S-doped mesoporous carbon nanostructures as electrocatalysts for oxygen reduction reaction in acid medium, *Appl. Catal. B Environ.* 203 (2017) 889–898.

[33] H. Shen, E. Gracia-Espino, J. Ma, K. Zang, J. Luo, L. Wang, S. Gao, X. Mamat, G. Hu, T. Wagberg, S. Guo, Synergistic effects between atomically dispersed fe – n – c and c – s – c for the oxygen reduction reaction in acidic media, *Angew. Chem. Int. Ed.* 56 (2017) 13800–13804.

[34] R. Jasinski, A New fuel cell cathode catalyst, *Nature* 201 (1964) 1212–1213.

[35] H. Jahnke, M. Schönborn, G. Zimmermann, Organic dyestuffs as catalysts for fuel cells, *Phys. Chem. Appl. Dyest.* 61 (1976) 133–181.

[36] V.S. Bagotzky, M.R. Tarasevich, K.A. Radyushkina, O.A. Levina, S.I. Andrusyova, Electrocatalysis of the oxygen reduction process on metal chelates in acid electrolyte, *J. Power Sources* 2 (2011) 233–240.

[37] J.A.R. van Veen, C. Visser, Oxygen reduction on monomeric transition metal phthalocyanines in acid electrolyte, *Adsorption* 24 (1979) 921–928.

[38] J.A.R. van Veen, J.F. van Baar, K.J. Kroese, Effect of heat treatment on the performance of carbon-supported transition-metal chelates in the electrochemical reduction of oxygen, *J. Chem. Soc. Faraday Trans. I* 77 (1981) 2827–2843.

[39] J.H. Zagal, M.T.M. Koper, Reactivity descriptors for the activity of molecular  $MN_4$  catalysts for the oxygen reduction reaction, *Angew. Chem. Int. Ed.* 55 (2016) 14510–14521.

[40] J.A.R. van Veen, H.A. Colijn, J.F. van Baar, On the effect of a heat treatment on the structure of carbon-supported metalloporphyrins and phthalocyanines, *Electrochim. Acta* 33 (1988) 801–804.

[41] N. Daems, X. Sheng, I.F.J. Vankelecom, P.P. Pescarmona, Metal-free doped carbon materials as electrocatalysts for the oxygen reduction reaction, *J. Mater. Chem. A* 2 (2014) 4085–4110.

[42] P. Giannozzi, S. Baroni, N. Bonini, M. Calandra, R. Car, C. Cavazzoni, D. Ceresoli, G.L. Chiarotti, M. Cococcioni, I. Dabo, A.D. Corso, S. De Gironcoli, U. Gerstmann, C. Gougaud, A. Kokalj, M. Lazzeri, L. Martin-samos, N. Marzari, F. Mauri, R. Mazzarello, S. Paolini, A. Pasquarello, L. Paulatto, C. Sbraccia, QUANTUM ESPRESSO : a modular and open-source software project for quantum simulations of materials, *J. Phys. Condens. Matter* 21 (2009) 395502–395521.

[43] B.J. Alder, Ground State of the electron gas by a stochastic method, *Phys. Rev. Lett.* 45 (1980) 566–569.

[44] J.P. Perdew, K. Burke, M. Ernzerhof, Generalized gradient approximation made simple, *Phys. Rev. Lett.* 77 (1996) 3865–3868.

[45] Z.Q. Li, C.J. Lu, Z.P. Xia, Y. Zhou, Z. Luo, X-ray diffraction patterns of graphite and turbostratic carbon, *Carbon* 45 (2007) 1686–1695.

[46] C.H. Choi, M.W. Chung, S.H. Park, S.I. Woo, Additional doping of phosphorus and/or sulfur into nitrogen-doped carbon for efficient oxygen reduction reaction in acidic media, *Phys. Chem. Chem. Phys.* 15 (2013) 1802–1805.

[47] S.-A. Wohlgemuth, F. Vilela, M.-M. Titirici, M. Antonietti, A one-pot hydrothermal synthesis of tunable dual heteroatom-doped carbon microspheres, *Green Chem.* 14 (2012) 741–749.

[48] H.B. Yang, J. Miao, S.-F. Hung, J. Chen, H.B. Tao, X. Wang, L. Zhang, R. Chen, J. Gao, H.M. Chen, L. Dai, B. Liu, Identification of catalytic sites for oxygen reduction and oxygen evolution in N-doped graphene materials: development of highly efficient metal-free bifunctional electrocatalyst, *Sci. Adv.* 2 (2016) e1501122–e1501122.

[49] Y. Zhang, P. Li, X. Yin, Y. Yan, K. Zhan, J. Yang, B. Zhao, Cobalt sulfide supported on nitrogen and sulfur dual-doped reduced graphene oxide for highly active oxygen reduction reaction, *RSC Adv.* 7 (2017) 50246–50253.

[50] S. Niu, W. Lv, G. Zhou, Y. He, B. Li, Q.-H. Yang, F. Kang, N and S co-doped porous carbon spheres prepared using L-cysteine as a dual functional agent for high-performance lithium-sulfur batteries, *Chem. Commun.* 51 (2015) 17720–17723.

[51] H. Ding, J.-S. Wei, H.-M. Xiong, Nitrogen and sulfur co-doped carbon dots with strong blue luminescence, *Nanoscale* 6 (2014) 13817–13823.

[52] A.L. Cazetta, A.C. Martins, O. Pezoti, K.C. Bedin, K.K. Beltrame, T. Asefa, V.C. Almeida, Synthesis and application of N-S-doped mesoporous carbon obtained from nanocasting method using bone char as heteroatom precursor and template, *Chem. Eng. J.* 300 (2016) 54–63.

[53] H.T. Yi, Y.Q. Zhu, X.Y. Chen, Z.J. Zhang, Nitrogen and sulfur co-doped nanoporous carbon material derived from p-nitrobenzeneamine within several minutes and the supercapacitor application, *J. Alloys Compd.* 649 (2015) 851–858.

[54] R.K. Shervedani, A. Amini, Carbon black/sulfur-doped graphene composite prepared by pyrolysis of graphene oxide with sodium polysulfide for oxygen reduction reaction, *Electrochim. Acta* 142 (2014) 51–60.

[55] R. Silva, D. Voiry, M. Chhowalla, T. Asefa, Efficient metal-Free electrocatalysts for oxygen reduction: polyaniline-derived N- and o-doped mesoporous carbons, *J. Am. Chem. Soc.* 135 (2013) 7823–7826.

[56] Q. Wei, X. Tong, G. Zhang, J. Qiao, Q. Gong, S. Sun, Nitrogen-doped carbon nanotube and graphene materials for oxygen reduction reactions, *Catalysts* 5 (2015) 1574–1602.

[57] Y. Shao, S. Zhang, M.H. Engelhard, G. Li, G. Shao, Y. Wang, J. Liu, I.A. Aksay, Y. Lin, Nitrogen-doped graphene and its electrochemical applications, *J. Mater. Chem.* 20 (2010) 7491–7496.

[58] S. Yang, L. Zhi, K. Tang, X. Feng, J. Maier, K. M??llen, Efficient synthesis of heteroatom (N or S)-doped graphene based on ultrathin graphene oxide-porous silica sheets for oxygen reduction reactions, *Adv. Funct. Mater.* 22 (2012) 3634–3640.

[59] F. Buckel, F. Effenberger, C. Yan, A. Gölzhäuser, M. Grunze, Influence of aromatic groups incorporated in Long-Chain alkanethiol self-assembled monolayers on gold, *Adv. Mater.* 12 (2000) 901–905.

[60] I. Herrmann, U.I. Kramm, J. Radnik, S. Fiechter, P. Bogdanoff, Influence of sulfur on the pyrolysis of COTMP as electrocatalyst for the oxygen reduction reaction, *J. Electrochem. Soc.* 156 (2009) B1283–B1292.

[61] Z. Yang, Z. Yao, G. Li, G. Fang, H. Nie, Z. Liu, X. Zhou, X. Chen, S. Huang, Sulfur-doped graphene as an efficient metal-free cathode catalyst for oxygen reduction, *ACS Nano* 6 (2012) 205–211.

[62] C. You, S. Liao, H. Li, S. Hou, H. Peng, X. Zeng, F. Liu, R. Zheng, Z. Fu, Y. Li, Uniform nitrogen and sulfur co-doped carbon nanospheres as catalysts for the oxygen reduction reaction, *Carbon* 69 (2014) 294–301.

[63] Z. Yang, H. Nie, X. Chen, X. Chen, S. Huang, Recent progress in doped carbon nanomaterials as effective cathode catalysts for fuel cell oxygen reduction reaction, *J. Power Sources* 236 (2013) 238–249.

[64] A.M. El-Sawy, I.M. Mosa, D. Su, C.J. Guild, S. Khalid, R. Joesten, J.F. Rusling, S.L. Suib, Controlling the active sites of sulfur-doped carbon nanotube-graphene nanolobes for highly efficient oxygen evolution and reduction catalysis, *Adv. Energy Mater.* 6 (2016) 1501966–1501977.

[65] X. Wang, J. Wang, D. Wang, S. Dou, Z. Ma, J. Wu, L. Tao, A. Shen, C. Ouyang, Q. Liu, S. Wang, One-pot synthesis of nitrogen and sulfur co-doped graphene as efficient metal-free electrocatalysts for the oxygen reduction reaction, *Chem. Commun.* 50 (2014) 4839–4842.

[66] I.-A. Choi, D.-H. Kwak, S.-B. Han, J.-Y. Park, H.-S. Park, K.-B. Ma, D.-H. Kim, J.-E. Won, K.-W. Park, Doped porous carbon nanostructures as non-precious metal catalysts prepared by amino acid glycine for oxygen reduction reaction, *Appl. Catal. B Environ.* 211 (2017) 235–244.

[67] Y. Jiao, Y. Zheng, M. Jaroniec, S.Z. Qiao, Origin of the electrocatalytic oxygen reduction activity of graphene-based catalysts: a roadmap to achieve the best performance, *J. Am. Chem. Soc.* 136 (2014) 4394–4403, <https://doi.org/10.1021/ja500432h>.

[68] J.J.-S. Moon, Y.-W. Lee, S.-B. Han, D.-H. Kwak, K.-H. Lee, A.-R. Park, J.I. Sohn, S.N. Cha, K.-W. Park, Iron–nitrogen-doped mesoporous tungsten carbide nanostructures as oxygen reduction electrocatalysts, *Phys. Chem. Chem. Phys.* 16 (2014) 14644–14650.

[69] S. Gupta, C. Pierro, E. Yeager, The effects of cyanide on the electrochemical properties of transition metal macrocycles for oxygen reduction in alkaline solutions, *J. Electroanal. Chem.* 306 (1991) 239–250.

[70] M.S. Thorum, J.M. Hankett, A.A. Gewirth, Poisoning the oxygen reduction reaction on carbon-supported Fe and Cu electrocatalysts: evidence for metal-centered

activity, *J. Phys. Chem. Lett.* 2 (2011) 295–298.

[71] J. Masa, W. Xia, M. Muhler, W. Schuhmann, On the role of metals in nitrogen-doped carbon electrocatalysts for oxygen reduction, *Angew. Chemie Int. Ed.* 54 (2015) 10102–10120.

[72] J. Liu, X. Sun, P. Song, Y. Zhang, W. Xing, W. Xu, High-performance oxygen reduction electrocatalysts based on cheap carbon black, nitrogen, and trace iron, *Adv. Mater.* 25 (2013) 6879–6883.

[73] W.J. Jiang, L. Gu, L. Li, Y. Zhang, X. Zhang, L.J. Zhang, J.Q. Wang, J.S. Hu, Z. Wei, L.J. Wan, Understanding the high activity of Fe-N-C electrocatalysts in oxygen reduction: Fe/Fe<sub>3</sub>C nanoparticles boost the activity of Fe-N<sub>x</sub>, *J. Am. Chem. Soc.* 138 (2016) 3570–3578.

[74] L. Yu, X. Pan, X. Cao, P. Hu, X. Bao, Oxygen reduction reaction mechanism on nitrogen-doped graphene: a density functional theory study, *J. Catal.* 282 (2011) 183–190.

[75] J. Song, T.F. Liu, S. Ali, B. Li, D.S. Su, The synergy effect and reaction pathway in the oxygen reduction reaction on the sulfur and nitrogen dual doped graphene catalyst, *Chem. Phys. Lett.* 677 (2017) 65–69.

[76] Z. Lu, S. Li, C. Liu, C. He, X. Yang, D. Ma, G. Xu, Z. Yang, Sulfur doped graphene as a promising metal-free electrocatalyst for oxygen reduction reaction: a DFT-D study, *RSC Adv.* 7 (2017) 20398–20405.

[77] D.R. Stull, H. Prophet, JANAF thermochemical tables, *Nat. Stand. Ref. Data Ser. Nat. Bur. Stand. (U.S.)* 37 (1971) 1141.

[78] H.T. Chung, D.A. Cullen, D. Higgins, B.T. Snead, E.F. Holby, K.L. More, P. Zelenay, Direct atomic-level insight into the active sites of a high-performance PGM-free ORR catalyst, *Science* 357 (2017) 479–484.

[79] J. Shui, C. Chen, L. Grabstanowicz, D. Zhao, D.-J. Liu, Highly efficient nonprecious metal catalyst prepared with metal–organic framework in a continuous carbon nanofibrous network, *Proc. Natl. Acad. Sci.* 112 (2015) 10629–10634.

[80] G. Zhang, R. Chenitz, M. Lefèvre, S. Sun, J. Dodelet, Is iron involved in the lack of stability of Fe/N/C electrocatalysts used to reduce oxygen at the cathode of PEM fuel cells? *Nano Energy* 29 (2016) 111–125.

[81] T. Sun, Q. Wu, Y. Jiang, Z. Zhang, L. Du, L. Yang, X. Wang, Sulfur and nitrogen codoped carbon tubes as bifunctional metal–free electrocatalysts for oxygen reduction and hydrogen evolution in acidic media, *Chem. A Eur. J. Commun.* 22 (2016) 10326–10329.

[82] Z. Liu, H. Nie, Z. Yang, J. Zhang, Z. Jin, Y. Lu, Z. Xiao, S. Huang, Sulfur–nitrogen co-doped three-dimensional carbon foams with hierarchical pore structures as efficient metal-free electrocatalysts for oxygen reduction reactions, *Nanoscale* 5 (2013) 3283–3288.

[83] Y.-C. Wang, Y.-J. Lai, L. Song, Z.-Y. Zhou, J.-G. Liu, Q. Wang, X.-D. Yang, C. Chen, W. Shi, Y.-P. Zheng, M. Rauf, S.-G. Sun, S-doping of an Fe/N/C ORR catalyst for polymer electrolyte membrane fuel cells with high power density, *Angew. Chem. Int. Ed.* 54 (2015) 9907–9910.